JOURNAL OF GEOPHYSICAL RESEARCH, VOL. 114, B02104, doi:10.1029/2008JB006017, 2009

Nanofabrication of two-dimensional arrays of magnetite particles for fundamental rock magnetic studies

David Krása,[1] Chris D. W. Wilkinson,[2] Nikolaj Gadegaard,[2] Xiang Kong,[3] Haiping Zhou,[2] Andrew P. Roberts,[4] Adrian R. Muxworthy,[5] and Wyn Williams[1]

Received 15 August 2008; revised 3 December 2008; accepted 18 December 2008; published 17 February 2009.

[1] Magnetic measurements of samples with precisely controlled magnetic mineralogy, grain size, and interparticle spacing are needed to provide crucial experimental rock magnetic underpinning for paleomagnetic studies. We report a novel nanofabrication method for producing two-dimensional arrays of cylindrical synthetic magnetite particles with well-defined composition, particle size, and interparticle spacing. The samples are fabricated by writing dot arrays with electron beam lithography, transferring these patterns into sputtered Fe thin films by reactive ion etching in a CO/NH_3 plasma, and oxidizing the resulting Fe particles in a controlled atmosphere to form magnetite. Scanning electron microscopy and transmission electron microscopy have been used to monitor the fabrication process and to determine the particle geometry. The particle sizes of our samples range between 100 nm and 265 nm with center-to-center spacings between 180 nm and 310 nm. Low-temperature magnetic remanence data confirm the stoichiometry of the magnetite. We present magnetic hysteresis data and first-order reversal curve diagrams for our samples and compare these with previously published data from other synthetic and natural magnetite samples. The ability to independently control particle size and interparticle spacing of magnetite grains makes our synthetic samples ideal for studying the influence of magnetostatic interactions on the paleomagnetic recording fidelity of naturally occurring magnetite in rocks.

Citation: Krása, D., C. D. W. Wilkinson, N. Gadegaard, X. Kong, H. Zhou, A. P. Roberts, A. R. Muxworthy, and W. Williams (2009), Nanofabrication of two-dimensional arrays of magnetite particles for fundamental rock magnetic studies, *J. Geophys. Res.*, *114*, B02104, doi:10.1029/2008JB006017.

1. Introduction

[2] Particle size, shape, interparticle spacing, and composition are important parameters that influence the magnetic properties of a given particulate magnetic material. In technological magnetic memory applications, these parameters are important because they control the stability and density of magnetic recording. However, understanding the properties of finely dispersed magnetic particles is also important in geophysics, where the properties of naturally occurring magnetic minerals affect the fidelity and stability of the paleomagnetic record contained in geological materials.

[3] In rocks, the most common ferrimagnetic or antiferromagnetic minerals are Fe oxides or Fe-Ti oxides, which have broad variations in particle size, shape and spacing. Generally, particles in the single domain (SD) grain size range are regarded as ideal paleomagnetic recorders because of their strong remanence and high magnetic stability, with relaxation times on the order of the age of the Earth ($>10^9$ years) [e.g., *Dunlop and Özdemir*, 1997]. Additionally, a thermoremanent magnetization carried by SD particles meets a number of conditions such as independence, additivity and linearity with applied field, that allow paleomagnetists to determine the absolute paleointensity of the Earth's past geomagnetic field [e.g., *Néel*, 1949; *Thellier and Thellier*, 1959; *Coe*, 1967]. However, rocks rarely contain ideal assemblages of monodisperse SD particles. Techniques used to determine the magnetic domain state of remanence carriers, such as plotting the ratio of saturation remanence over saturation magnetization (M_{RS}/M_S) versus the ratio of coercivity of remanence over coercive force (B_{CR}/B_C) [*Day et al.*, 1977], or determining first-order reversal curve (FORC) diagrams [*Pike et al.*, 1999; *Roberts et al.*, 2000], often reveal the presence of a mixture of SD and multidomain (MD) particles, or of pseudosingle-domain (PSD) particles [e.g., *Dunlop*, 2002; *Carvallo et al.*, 2006]. These larger particles generally have a lower magnetic stability than SD particles and can lead to erroneous determinations of absolute paleointensity [e.g., *Krása et al.*, 2003; *Leonhardt et al.*, 2004].

[1]School of GeoSciences, University of Edinburgh, Edinburgh, UK.
[2]James Watt Nanofabrication Centre, Department of Electronics and Electrical Engineering, University of Glasgow, Glasgow, UK.
[3]Department of Physics and Astronomy, University of Glasgow, Glasgow, UK.
[4]National Oceanography Centre, University of Southampton, Southampton, UK.
[5]Department of Earth Science and Engineering, Imperial College, London, UK.

0148-0227/09/2008JB006017$09.00

[4] Natural magnetic minerals also often occur as dense intergrowths or as exsolution structures with narrow particle spacing, which give rise to magnetostatic interactions among particles [e.g., *Harrison et al.*, 2002; *Feinberg et al.*, 2005; *Evans et al.*, 2006]. These interactions affect the stability of magnetic remanence as well as determinations of magnetic domain state. However, quantifying the influence of magnetostatic interactions on paleomagnetic data is notoriously difficult because of the complex interplay between particle size, shape and spacing and because of the wide variation of these parameters in natural samples.

[5] In order to study systematically the influence of these parameters on magnetic properties, we describe a nanofabrication method using electron beam lithography (EBL) that enables production of magnetic particle assemblages with well-defined composition and particle geometry. EBL is widely used in microelectronics to produce integrated circuits, and is increasingly being used in interdisciplinary research such as nanobiology and nanochemistry. In particular, we focus on magnetite because it is one of the most common and best studied terrestrial magnetic minerals, with a strong specific saturation magnetization of 92 A m^2 kg^{-1}. Interparticle spacing is an important factor for strongly magnetic minerals such as magnetite because close spacing can give rise to magnetostatic interactions among particles. This will, in turn, influence the magnetic recording fidelity of magnetic particle assemblages.

[6] Fabrication of patterned magnetic mineral samples by EBL was previously employed to study iron oxides by *King et al.* [1996]. The EBL tool used in that study limited the writing area to less than 1 mm^2. Consequently, the magnetic signal measured in bulk magnetic measurements for these samples was relatively weak. For the present work, two dedicated EBL tools were available, allowing writing of sample areas of 25 mm^2 and above. *King et al.* [1996] used the additive technique and liftoff to transfer the pattern into the magnetic layer. This was adequate for the small square areas fabricated then: however, this process makes it difficult to produce large patterned areas of small particles without defective areas.

[7] In this study, we chose to develop a reactive ion etching (RIE) process for pattern transfer to fabricate large two-dimensional arrays of magnetite (Fe_3O_4) particles with grain sizes in the range of tens to hundreds of nanometers. In addition to the large patterned areas that can be reliably transferred into the magnetic material, RIE has the advantage over the liftoff process of a better sidewall profile; that is, the individual particles ideally have almost vertical sidewalls. With the liftoff process, particles are more cone shaped. Our aim is to produce samples with a range of well-defined particle sizes and interparticle spacings to systematically study the influence of magnetostatic interactions on the micromagnetic structure and bulk magnetic properties. We report here the fabrication process and magnetic properties of the first samples fabricated using this process.

2. Fabrication Process

[8] The basic principle of EBL particle array fabrication as described here is to write the desired particle pattern (in this case a dot pattern) with an electron beam into a layer of electron sensitive material (the resist) on top of a thin film of magnetic material that will later form the particle array. The resist layer is then developed, similar to a photographic film. Depending on the type of resist (negative or positive), either the parts exposed to electrons or the ones not exposed to electrons, remain to form a mask layer. In the following transfer process, this mask pattern serves to protect the underlying magnetic thin film so that an etching process can be used to selectively remove parts of the thin film that are not covered by resist. Depending on the etch resistance of the resist, an intermediate layer of a sacrificial material (hard mask) can be deposited on top of the magnetic thin film, which serves to increase the durability of the mask during the etching process. The complete fabrication process used in this study is schematically shown in Figure 1.

2.1. Sputtering

[9] The starting materials for the fabrication process are radio frequency (RF) sputtered Fe thin films (Figure 1a). We used 99.99% pure Fe targets under the following sputtering conditions: Ar flow rate of 34 mPa m^3 s^{-1} (20 sccm), power of 250 W, and a DC bias voltage of 1000 V. Si wafers with (100) orientation were used as substrates, with Fe deposition at a rate of 10 nm min^{-1}. The deposited Fe film is polycrystalline, with a typical crystallite size of around 10–20 nm. The thickness and quality of the deposited Fe film were monitored with a Dektak profilometer, by measuring the sheet resistance, and by acquiring cross-sectional SEM images (Figure 1g). The sheet resistance generally varies by ±5% of the total value over the area of a wafer with 10 cm diameter. On the length scale of individual samples (edge length typically less than 5 mm), the Fe films are essentially homogeneous in terms of thickness and composition.

2.2. EBL Resist

[10] In order to reach the ideal SD grain size range of magnetite (tens of nanometers), a high-resolution EBL resist is required. We used hydrogen silsesquioxane (HSQ) [*Namatsu et al.*, 1998], a negative tone inorganic electron beam resist, because of its high-resolution and etch resistance. Depending on the required grain size, the samples were spin coated with HSQ films to a thickness of between 80 and 140 nm (Figures 1a and 1g). The samples were then prebaked at 77°C for 2 min on a hot plate and the desired dot pattern was written with either a Leica EBPG5 beam writer or a VB6 EBL tool at the James Watt Nanofabrication Centre at Glasgow University (Figure 1b). The HSQ resist was developed in 25% tetramethylammonium hydroxide (TMAH) at 23°C for 4 min followed by rinsing in water and isopropanol (Figures 1c and 1h).

2.3. Pattern Design and Exposure

[11] In order to reduce the writing time for the required large area dot patterns, we used a single spot electron beam writing technique [*Gadegaard et al.*, 2003] in which a single exposure with a focused Gaussian beam defines the shape of the desired circular dots. The whole dot pattern is designed as a rectangle, the spot size is chosen according to the desired dot size, and, in contrast to conventional EBL, the beam step size is larger than the spot size and so defines the distance between the dots. In this study, we only produced rectangular dot arrays, but, in principle, any pattern design is feasible. In particular, methods for the

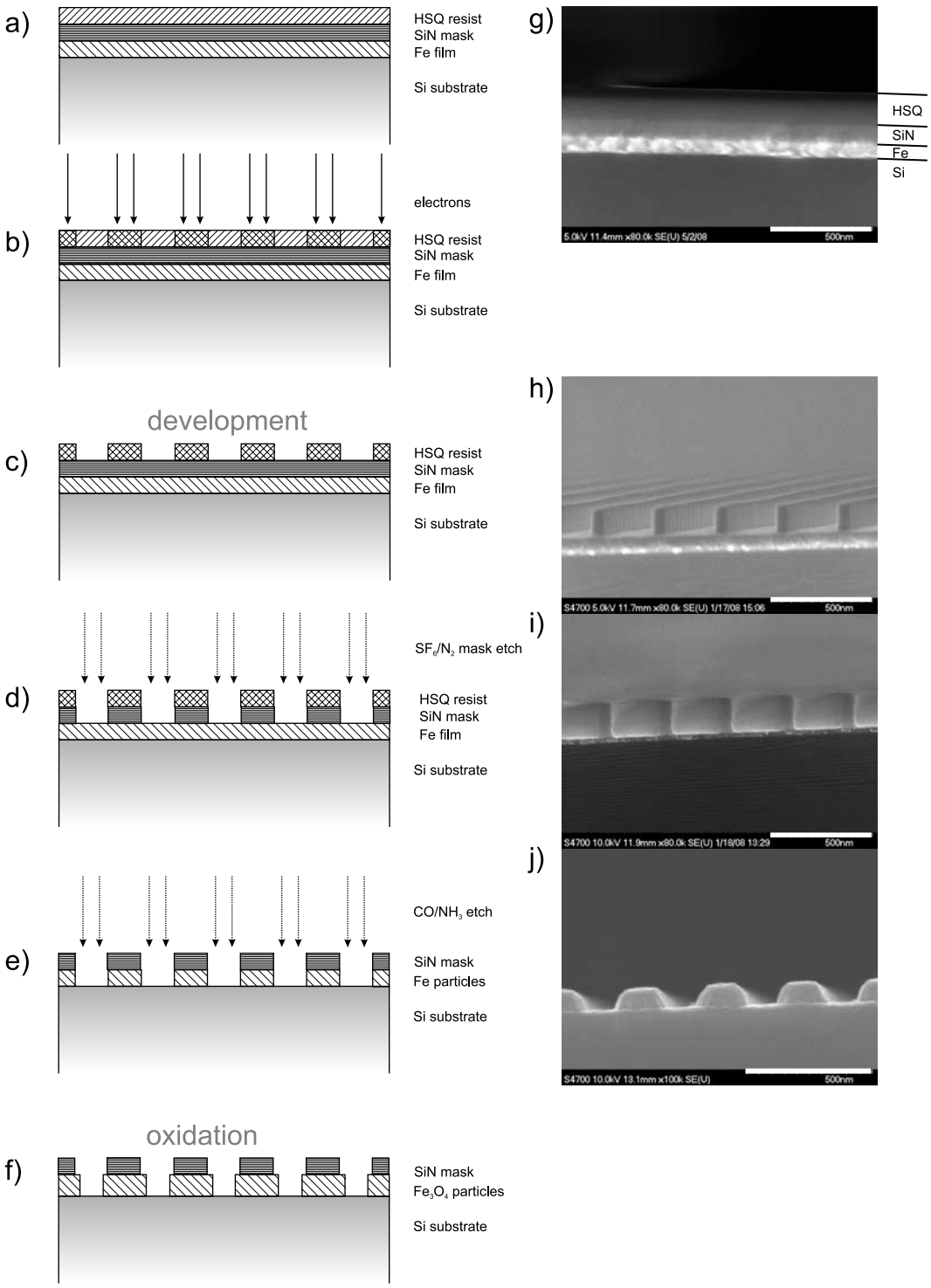

Figure 1. Processing steps in the fabrication of two-dimensional arrays of magnetite particles with (a–f) schematic drawings of the various steps and (g–j) cross-sectional SEM images after selected processing steps. The process as shown here involves the use of a SiN hard mask layer between the Fe thin film and the HSQ resist layer (see text).

generation of hexagonal dot arrays and randomly positioned dots have been developed [*Curtis et al.*, 2004; *Dalby et al.*, 2007; *Gadegaard et al.*, 2008].

[12] Typical examples of HSQ dot patterns on Fe film are shown in Figure 2. The dot size can be controlled both by the electron spot size as well as by electron dose. The ideal doses for each spot size were determined by varying the exposure dose and measuring the resulting dot size.

2.4. Pattern Transfer by Dry Etching

[13] The dot patterns in HSQ were transferred into the Fe layer by RIE in CO/NH_3 plasma using an Electrotech

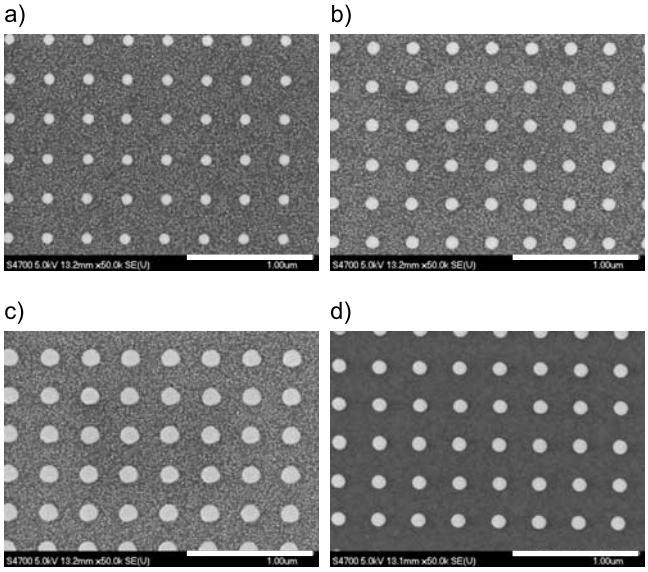

Figure 2. Dot patterns in HSQ after electron beam exposure and development. All four patterns were written with a Leica EBPG5 beam writer with the same electron spot size (diameter of Gaussian beam) of 56 nm and a beam step size of 312 nm but with varying electron doses. The polycrystalline nature of the Fe thin film beneath the HSQ pattern is clearly visible in Figures 2a–2c. The average grain size of Fe crystallites is approximately 20 nm. For comparison, Figure 2d is an HSQ pattern on a sample with an additional SiN hard mask layer between the Fe thin film and the HSQ layer. Electron doses in μC cm^{-2} were (a) 200, (b) 346, (c) 600, and (d) 397.

ET340 RIE tool (Figures 1e and 1j). The CO/NH_3 fabrication route was introduced to etch Fe-Ni alloys and Co for magnetic memory applications [*Nakatani*, 1996; *Matsui et al.*, 2002]. The process is believed to combine physical sputtering with the formation of volatile Fe-carbonyl compounds. We employed a similar process for Fe as well as Fe-Ni etching [*Kong et al.*, 2008]. The CO/NH_3 flow ratio amounts to 13.5 mPa m^3 s^{-1}/20.3 mPa m^3 s^{-1} (8 sccm/12 sccm) at an RF power of 100 W. The process pressure varied between 1.7 and 3.7 Pa (13–28 mtorr). Etching was carried out at room temperature. We found that the etching rate is highly variable. The etching progress was therefore always monitored by laser reflectometry [*Khamsehpour et al.*, 1997] to ensure that the Fe layer was fully etched. A theoretical reflectance profile was calculated on the basis of the model of *Hicks et al.* [1994]. There is good agreement between the calculated and measured development of reflectance in the course of the etching process (Figure 3). The initially low reflectance in the experimental data is probably due to an oxidized Fe surface layer. Fe etch rates vary between 1 and 6 nm min^{-1}, and the HSQ resist etch rate is 4 nm min^{-1}.

[14] Because of this low selectivity (i.e., low ratio of Fe etch rate over resist etch rate), we also studied an alternative pattern transfer route, that of adding an additional SiN hard mask layer between the Fe thin film and HSQ resist layer (Figures 1a, 1g, and 2d). The SiN layer was deposited at room temperature by inductively coupled plasma enhanced chemical vapor deposition (ICP-CVD) in an Oxford System 100 deposition machine [*Zhou et al.*, 2006]. After HSQ development, the SiN layer was etched in SF_6/N_2 plasma at flow rates of 8.4 mPa m^3 s^{-1} (5 sccm) and 92.9 mPa m^3 s^{-1} (55 sccm), respectively, RF power of 20 W and a process pressure of 2.0 Pa (15 mtorr) (Figures 1d and 1i). This etch was done in an Oxford System 100 RIE tool. The sample was then transferred to the ET340 RIE tool to proceed with the CO/NH_3 process as detailed above. The etch rate of SiN in SF_6/N_2 is 16 nm min^{-1} and the etch rate of SiN in CO/NH_3 is 1.3 nm min^{-1}. Comparing this latter value with the etch rate of Fe in CO/NH_3 yields a selectivity of between 0.8 and 4.6 with respect to Fe. An example of a successful pattern transfer into the Fe thin film is shown in Figure 4a. The starting material for this sample was an 80-nm-thick Fe film with a 60 nm SiN hard mask layer and 140 nm of HSQ resist. The pattern was written with the 56 nm spot of the EBPG5 beam writer and a beam step size of 312 nm.

2.5. Oxidation

[15] The final fabrication step involved oxidation of the patterned Fe thin film under controlled oxygen fugacity to

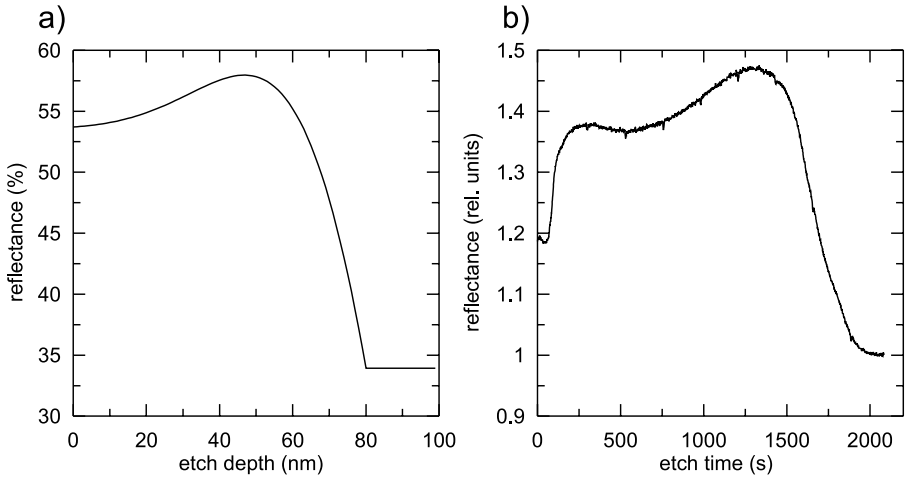

Figure 3. Plots of (a) modeled reflectance versus etch depth and (b) measured reflectance versus etch time for a 80 nm Fe layer on Si etched in a CO/NH_3 plasma.

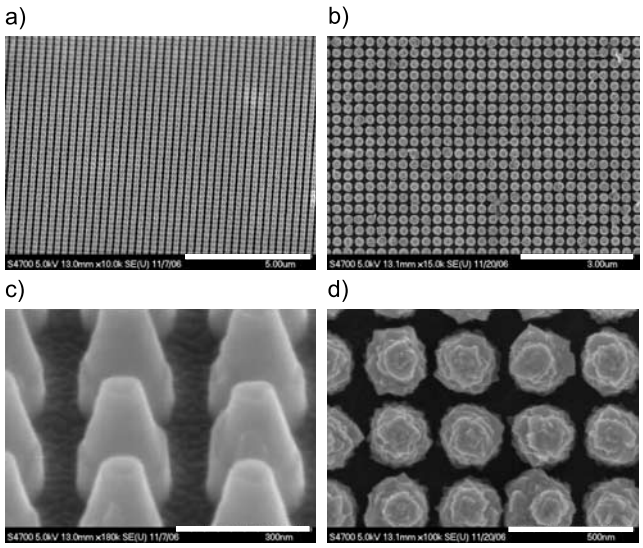

Figure 4. SEM images of sample DK0011 after Fe etching in a CO/NH_3 plasma at (a) low and (c) high magnification viewed at an oblique angle, and SEM images of the same sample after oxidation at 600°C in a controlled CO_2/H_2 atmosphere at (b) low and (d) high magnification. The irregular structures on top of the oxidized particles are residuals of the HSQ resist layer (Figure 4d).

convert it to stoichiometric magnetite (Figure 1f). Oxidation was carried out at 600°C in a H_2/CO_2 atmosphere with a concentration of 6% H_2 (by mass). An example of a final oxidized sample is shown in Figure 4b. Oxidation changes the crystal structure and increases the volume of the final magnetite particles by a factor of about 2.1 with respect to the unoxidized iron particles, thus increasing the diameter of particles by about 1.3. This, on the one hand, limits the minimum attainable grain size, but, on the other hand, allows production of samples with small intergrain spacing. After controlled oxidation, the samples were stored in isopropanol to minimize chemical alteration.

3. Microscopic and Microanalytical Characterization

[16] After each fabrication step, the samples where inspected with a Hitachi S4700 scanning electron microscope (SEM) with attached energy dispersive X-ray analysis (EDX) detector. Images acquired after each fabrication step are shown in Figures 1, 2, 4, and 5. Complete etching of the Fe film was ensured by inspecting cross sections of the samples and identifying the Si substrate, Fe layer and resist using the SEM (Figure 5). The success of the etching process was also checked by acquiring EDX spectra within and outside the patterned area. The absence of Fe peaks outside the patterned area was judged to be a positive test of the etching process (Figure 6). SEM images of the final magnetite particle arrays were used to determine the average volume of the particles and the total mass of magnetite for each sample. This was done with the image processing software package ImageJ [*Abramoff et al.*, 2004].

[17] A bright field cross-sectional TEM image of one of the nanofabricated Fe particles is shown in Figure 7a (before oxidation). It is clearly visible that the Fe film surrounding the desired particle was completely etched down to the Si substrate. A slight over-etch is visible with the Si substrate surface being slightly lower in the area around the particle than directly below it. The dark patches directly below the Si surface indicate diffraction contrast in these areas, which is most likely caused by radiation damage of, or ion implantation into, the Si substrate. This will not affect the magnetic properties of the samples. Figure 7b is a high-resolution close-up of the same particle in which individual atom columns can be seen in the Si substrate. No direct alignment between the crystallographic axes of the Fe particles and the Si substrate can be identified in this image. On the basis of this observation, and because

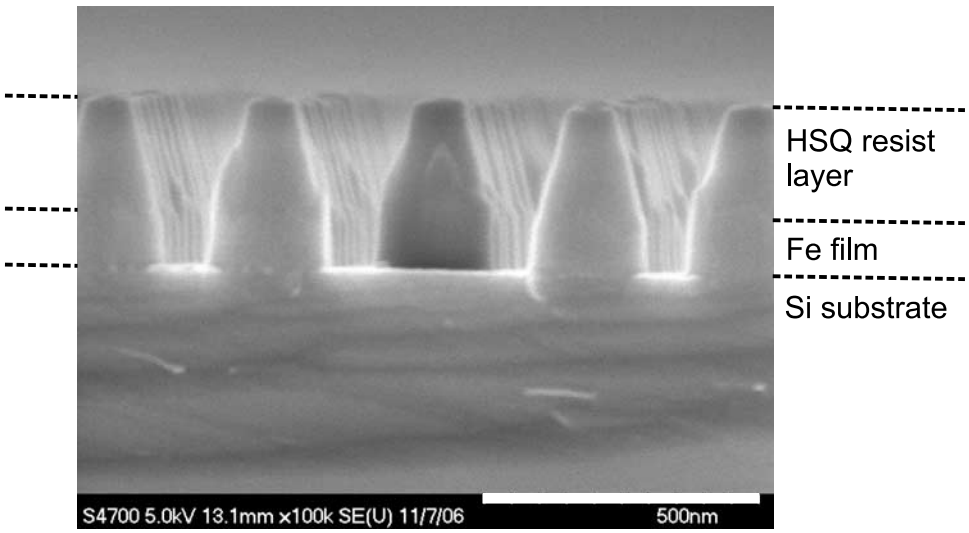

Figure 5. SEM image of a cross section of sample DK0011 after Fe etching in a CO/NH_3 plasma. The Si substrate can be distinguished from the Fe film by the staggered cleavage planes that are present in the substrate but that are not present in the Fe film. At the interface between the Fe film and the HSQ resist, a change in etching profile is evident as a more vertical etch in the Fe.

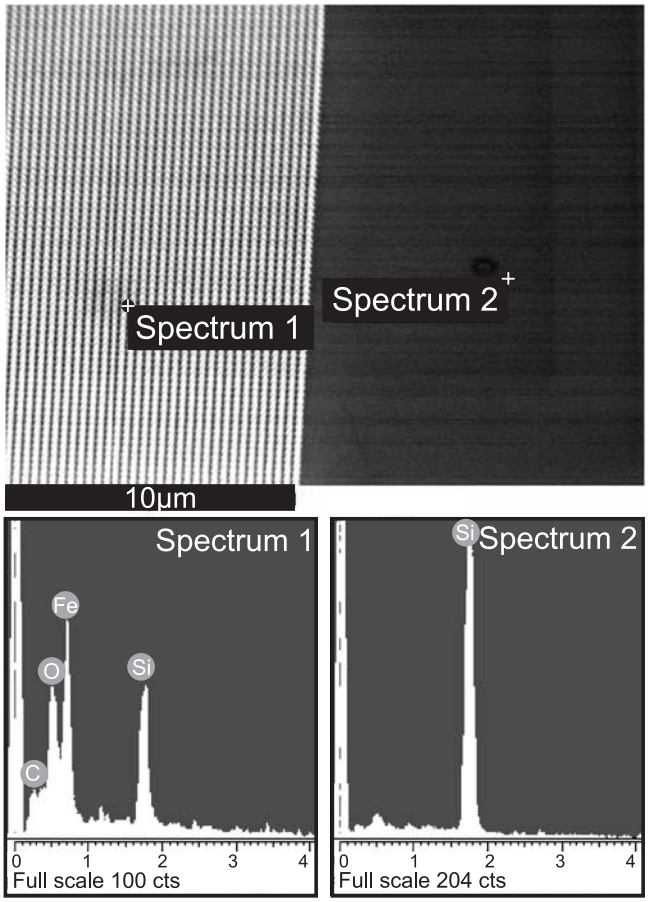

Figure 6. EDX spectra and measurement locations within and outside the patterned area demonstrate complete etching of the Fe film.

the particles recrystallize during oxidation, we assume that the resulting magnetite particles are randomly oriented.

4. Magnetic Characterization

[18] Three nanofabricated samples with grain sizes between 100 nm and 265 nm and with center-to-center particle spacings between 180 nm and 310 nm have been studied with a range of magnetic methods. The results of these measurements are summarized in Table 1.

4.1. Low-Temperature Magnetic Remanence Curves

[19] Low-temperature magnetic remanence measurements were carried out to confirm the stoichiometry of the final magnetite particles. Magnetite has a prominent low-temperature crystallographic phase transition where the crystal symmetry changes from cubic above the Verwey transition (T_V, [*Verwey*, 1939]) to monoclinic below T_V. The temperature of this transition is 125 K for "perfect" magnetite [*Walz*, 2002]. However, the magnitude of the transition, and the temperature at which it occurs, are sensitive to the presence of lattice vacancies, oxidation, or substitution of Fe by other cations such as Al or Ti. Generally, minor lattice vacancies or cation substitution will decrease T_V. With higher degrees of nonstoichiometry or surficial oxidation, the transition disappears altogether. Low-temperature saturation isothermal remanent magnetization (LT-SIRM) heating curves after cooling in a 2.5 T magnetic field (i.e., a field-cooled (FC) LT-SIRM) for our patterned magnetite samples (Figure 8) were measured on a Quantum Design Magnetic Properties Measurement System (MPMS). T_V was estimated by determining the maximum of d^2m/dT^2 from these curves (Table 1). T_V for the three samples lies between 114 and 115 K (Table 1). These temperatures agree well with previously published data from similarly sized stoichiometric magnetite [*Özdemir et al.*, 1993; *Smirnov*, 2006]. This confirms the near stoichiometric composition of the nanofabricated magnetite particles. FC LT-SIRM curves for sample DK0023 were repeatedly measured over the course of 7 days after oxidizing the sample to monitor for possible sample alteration due to surface maghemitization. The $m(T)$ curves and T_V did not change and we therefore rule out any significant magnetic mineral alteration of our samples after oxidizing them in a controlled atmosphere.

4.2. Magnetic Hysteresis Measurements

[20] Magnetic hysteresis loops and backfield demagnetization curves for the three samples were measured on a Princeton Measurements Corporation alternating gradient magnetometer (AGM) up to a maximum field of 1 T. The samples were mounted so that the external field was applied in the plane of the samples, and B_{CR}, M_{RS}/M_S, and B_C were determined (Figure 9 and Table 1). The mass of magnetite in each sample was calculated using the total volume of magnetite particles from the sample geometry and multiplying that with the density of magnetite. Measured M_S values range from 91 to 96 A m^2 kg^{-1}, which agrees well within error margins with the expected value of 92.4 A m^2 kg^{-1} [e.g., *Dunlop and Özdemir*, 1997]. Parameters affected by magnetite grain size, such as M_{RS}/M_S, and B_{CR}/B_C, lie within the expected range for PSD magnetite particles (Figure 10) [cf. *Day et al.*, 1977]). Note, however, that these parameters are expected to be strongly dependent on the field orientation with regard to the sample. Strictly speaking, the plot of *Day et al.* [1977] assumes isotropic samples, whereas our samples are highly anisotropic due to their two-dimensional nature.

4.3. First-Order Reversal Curve Diagrams

[21] The coercivity distribution and magnetostatic interaction fields of the samples were further characterized using FORC diagrams [*Pike et al.*, 1999; *Roberts et al.*, 2000] at room temperature on the same AGM used for hysteresis measurements (Figure 11). The FORC diagrams were

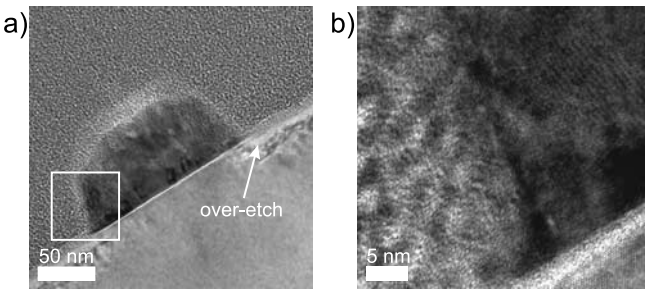

Figure 7. (a) Cross-sectional bright field TEM image of a nanofabricated Fe particle. (b) Enlargement of the area indicated by the white square in Figure 7a.

Table 1. Bulk Magnetic Parameters for Magnetite Samples Produced in This Study[a]

Sample	Dot Diameter (nm)	Separation (nm)	Dot Height (nm)	M_S (A m^2 kg^{-1})	M_{RS}/M_S	B_C (mT)	B_{CR} (mT)	B_{CR}/B_C	σ_{hys}	E_{hys} (A m^2 T kg^{-1})	B_{int} (mT)	T_V (K)	Pattern Area (mm^2)
DK0011	265 ± 13	310	192	92.2 ± 10	0.28	17.1	39.4	2.3	−0.21	5.12	35.3	115	1.3 × 2.0
DK0023	100 ± 6	310	102	91.0 ± 12	0.30	15.9	32.1	2.0	−0.33	4.18	14.5	115	4.0 × 4.0
DK0024-2	120 ± 15	180	102	96.0 ± 27	0.50	29.9	40.2	1.3	−0.37	7.95	13.2	114	3.5 × 3.5

[a]The dot separation is given as the center-to-center distance between adjacent particles. The shape parameter σ_{hys} and total hysteresis area E_{hys} are as defined by *Fabian* [2003]. The interaction field B_{int} is based on the full width at half maximum (FWHM) of a vertical profile through the FORC distribution as detailed in the text.

processed using the FORCObello software [*Winklhofer and Zimanyi*, 2006]. A first-order interpretation states that the horizontal spread in FORC diagrams provides a measure of the coercivity distribution of the sample, whereas the vertical spread is a measure of the interaction field strength [*Muxworthy and Roberts*, 2007].

[22] The measurements were carried out with the magnetic field applied in the plane of the samples. Sample DK0024-2 has an isolated maximum at B_C = 37 mT (Figure 11). The data for sample DK0023 are much noisier and the coercivity distribution is broader with a maximum at B_C = 30 mT. The full width at half maximum (FWHM) of a vertical profile through the maximum of the coercivity distribution is commonly chosen to quantify the interaction field B_{int}. To estimate the interaction field for sample DK0011, whose FORC distribution does not have an isolated peak, we took a vertical profile through the B_C value determined from the hysteresis loop. B_{int} values for the three samples are given in Table 1. Sample DK0011 has the largest B_{int} value of 35.3 mT, with samples DK0023 (B_{int} = 14.5 mT) and DK0024-2 (B_{int} = 13.2 mT) having B_{int} values that are less than half that for sample DK0011. Relatively strong magnetostatic interactions are expected for the geometry of sample DK0011 with its narrow particle spacing. The difference in B_{int} between samples DK0023 and DK0024-2 is relatively small, which was unexpected given the large difference in interparticle spacing for the two samples and their similar particle size. This is further discussed below. Only sample DK0024-2 has a pronounced negative area in the FORC distribution at negative B_b values. This negative area and the positive peak along the coercivity axis are approximately antisymmetrical about $B_b = -B_C$, as predicted by *Newell* [2005] for noninteracting SD grains dominated by uniaxial anisotropy and as explained by *Muxworthy and Roberts* [2007]. Numerical models for noninteracting SD grains dominated by cubic anisotropy do not produce this negative region [*Muxworthy et al.*, 2004].

5. Discussion

[23] While the initial steps of our fabrication route up to the etching of the SiN hard mask consist of standard nanofabrication procedures, the use of CO/NH_3 for etching of pure Fe thin films has not, to our knowledge, been studied previously. The general problem in etching magnetic thin films involving Fe, Ni, and Co is that there are not many volatile transition metal compounds. This is an essential condition for successful dry etching because the resulting products formed from the chemical reactions in the etching chamber must be removed by a vacuum pump. In the case of Fe in particular, Fe-pentacarbonyl ($Fe(CO)_5$) is likely to form during CO/NH_3 dry etching, which has a boiling point of 103°C. The process pressure reached during etching may therefore be an important parameter. Our records of dry etching runs indicate that the varying etch rate (1–6 nm min^{-1}) encountered in the fabrication process is mainly due to the varying process pressure of 1.7–3.7 Pa (13–28 mtorr). Successful etch runs (i.e., those in which the selectivity of the etching process was high enough to completely etch through the Fe film before the mask layer was fully eroded) were carried out at process pressures

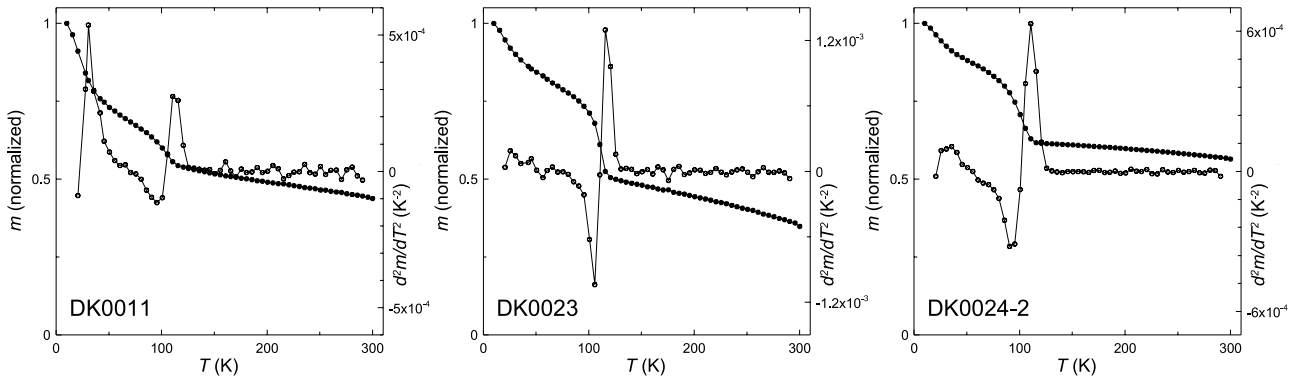

Figure 8. Remanent magnetization versus temperature during warming of a saturation isothermal remanent magnetization acquired at 10 K (FC LT-SIRM) acquired after cooling in a magnetic field of 2.5 T for the three samples produced for this study (left-hand axis, filled circles). The decrease in magnetization at around 115 K marks the Verwey transition. The second derivative d^2m/dT^2 is shown on the right-hand axis (open circles).

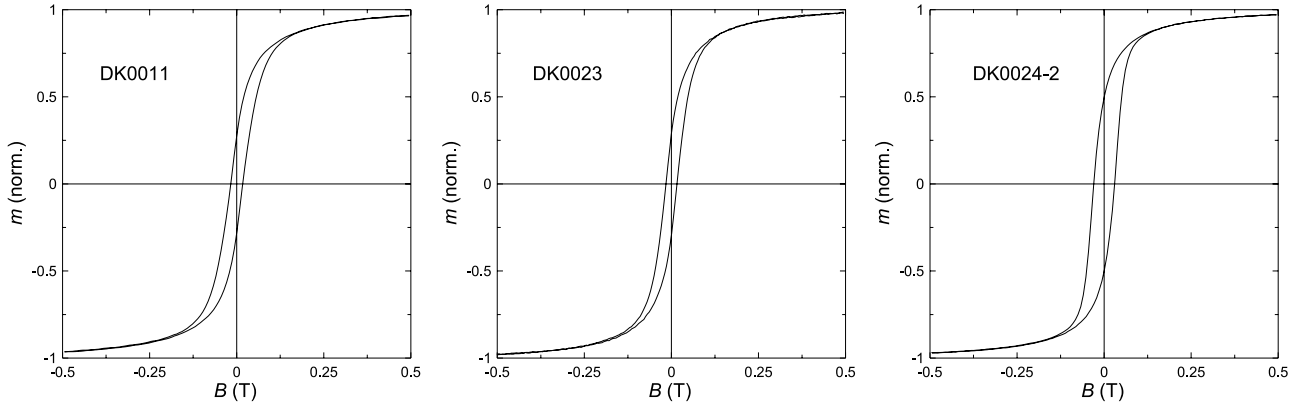

Figure 9. Hysteresis loops for the three studied nanofabricated samples measured in a maximum field of 1 T. Results are only shown for ±0.5 T (for greater detail).

below 2.3 Pa (17 mtorr). This is confirmed by previous studies where a steep decrease in Fe-Ni etch rates was observed with increasing pressure [*Nakatani*, 1996].

[24] Better patterning results are obtained with a SiN hard mask layer between the Fe film and HSQ resist layer. The SiN layer increases the selectivity of the CO/NH_3 dry etching process and provides a smoother interface for spinning on the HSQ resist than the underlying Fe thin film alone (see Figure 2d). This improves resist adhesion and makes smaller particle sizes achievable.

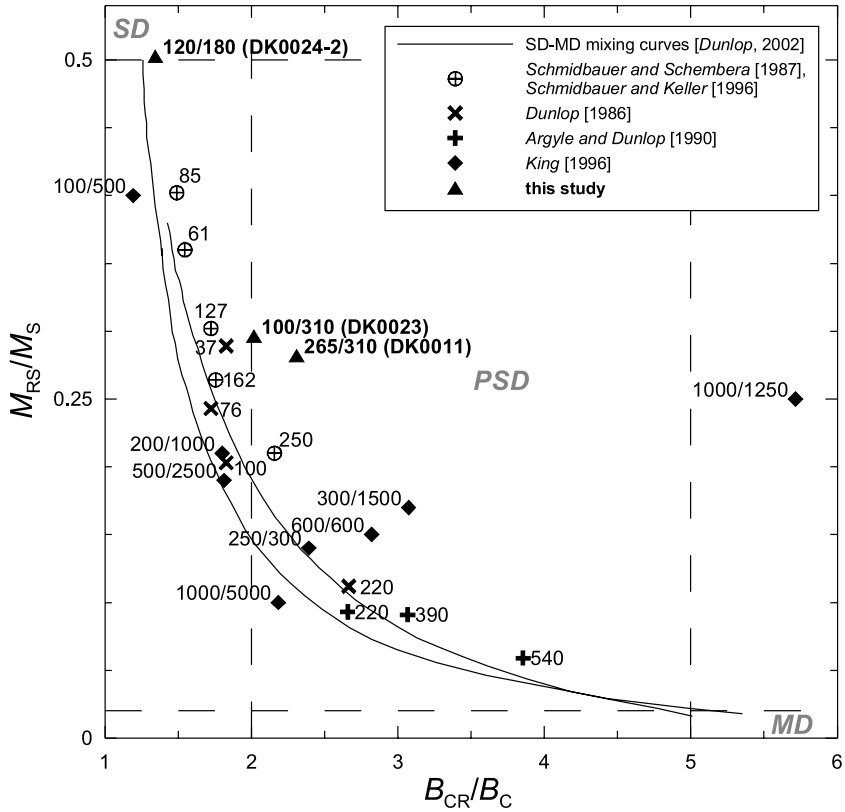

Figure 10. Plot of M_{RS}/M_S versus B_{CR}/B_C [cf. *Day et al.*, 1977] for nanofabricated samples from this study (solid triangles) compared with published data for previously nanofabricated magnetites [*King*, 1996], for magnetites precipitated from aqueous solution [*Dunlop*, 1986], for magnetites prepared by reducing hematite [*Argyle and Dunlop*, 1990], and for magnetites synthesized chemically by decomposition of oxalates followed by reduction [*Schmidbauer and Schembera*, 1987; *Schmidbauer and Keller*, 1996]. Grain sizes are shown in nm next to each data point. For data from this study, the first number indicates the grain size, the second number is the particle spacing (center to center), while the sample name is given in parentheses. SD-MD mixing curves and subdivision into SD, PSD, and MD regions are drawn after *Dunlop* [2002].

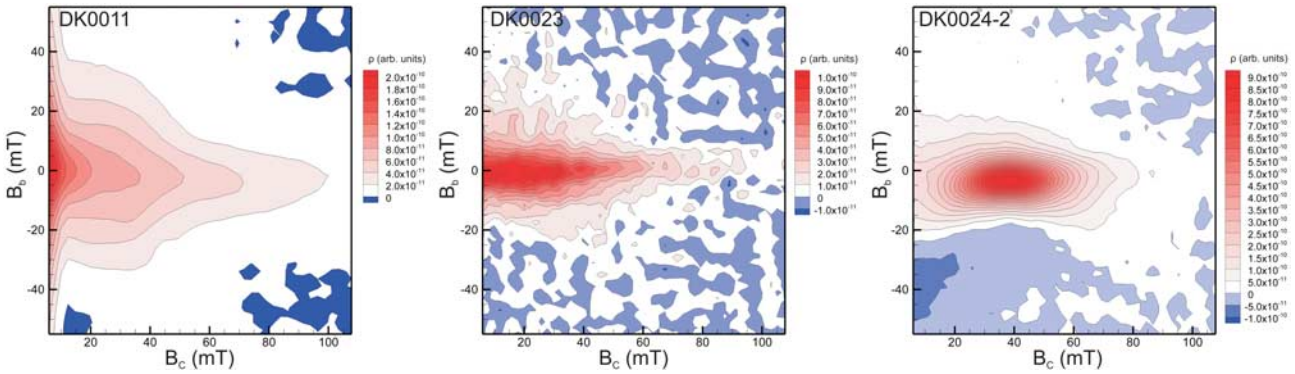

Figure 11. FORC distributions $\rho(B_b, B_C)$ for the three studied samples. The following smoothing factors (SF) were used to process the data: DK0011 (SF = 5), DK0023 (SF = 3), and DK0024-2 (SF = 3). The averaging time was 100 ms for all three samples. The choice of smoothing factor does not significantly affect B_{int}.

[25] M_{RS}/M_S versus B_{CR}/B_C values from our samples are compared to data for samples with a similar size range from other studies in Figure 10. Data for our nanofabricated samples generally fall into the field for small PSD particles. Our data are shifted toward higher M_{RS}/M_S values compared to similarly sized magnetites that were precipitated from aqueous solution [*Dunlop*, 1986]. The same trend is visible for the nanofabricated magnetites of *King* [1996] and for magnetites prepared by oxalate decomposition and reduction [*Schmidbauer and Schembera*, 1987]. For the latter samples, *Dunlop* [2002] mentioned three possible reasons for this shift: a distribution of grain sizes rather than a consistent single particle size, irregular particle shapes, and higher strains. The first two can be ruled out for the nanofabricated magnetite arrays, which leaves a higher level of strain as a possible cause, which is probably brought about by a higher lattice defect density than in samples produced via aqueous precipitation. The higher defect density and associated strains may also be the reason for the slight deviation of T_V from the expected value. A definitive reason for the relatively high M_{RS}/M_S values of our samples can only be given once the hysteresis parameters are measured in different directions with respect to the sample plane. However, regarding the mineralogical processes during fabrication, our samples are more similar to those of *Schmidbauer and Schembera* [1987] than to those formed by aqueous precipitation.

[26] The M_{RS}/M_S value of 0.5 for sample DK0024-2, which has a grain size of 120 nm and an interparticle spacing of 180 nm, is considerably higher than that of sample DK0023, which has a smaller grain size of 100 nm and a wider spacing of 310 nm. On the basis of micromagnetic models, we expect that noninteracting magnetite particles with grain sizes between 100 and 300 nm have a vortex-like micromagnetic structure; that is, they have PSD-like hysteresis behavior with M_{RS}/M_S values significantly below 0.5 [*Williams and Dunlop*, 1995]. However, in the case of sample DK0024-2, with its narrowly spaced particles, hysteresis properties are likely to be influenced by magnetostatic interactions in addition to the effects of higher defect density as discussed above. Interactions have been shown to increase the SD-MD threshold size for one-dimensional arrays (chains) of magnetite particles in this size range, thus increasing the M_{RS}/M_S ratio [*Muxworthy and Williams*, 2006a]. Models of magnetostatically interacting, three-dimensional array assemblages of 100 nm and 150 nm magnetite particles produce a similar result due to the formation of supervortex states [*Muxworthy et al.*, 2003]. Again, these interaction effects will strongly depend on measurement direction for our two-dimensional array samples.

[27] As mentioned above, FORC diagrams for samples DK0023 and DK0024-2, which have similarly sized particles but different interparticle spacings, do not have significantly different B_{int} values and thus do not seem to confirm magnetostatic interaction as the likely cause for the high M_{RS}/M_S values of sample DK0024-2. Decreasing interparticle spacing in systems of 1-μm PSD particles was shown to cause a shift of the peak in FORC distributions to lower coercivities and a widening of the distribution along the vertical axis [*Muxworthy et al.*, 2006]. The less densely spaced particles of sample DK0023 (diameter 100 nm, center-to-center spacing 310 nm) have a lower coercivity and a similar B_{int} compared to sample DK0024-2 (diameter 120 nm, center-to-center spacing 180 nm). One possible explanation for this apparent contradiction might be that the particles in sample DK0024-2 are in a grain size range where, in the absence of interactions, the vortex configuration is the energetically favorable micromagnetic state. However, because of the relatively narrow particle spacing, a supervortex state, as described by *Harrison et al.* [2002] and *Evans et al.* [2006] for a natural magnetite-ulvöspinel intergrowth might be the more favorable configuration when magnetostatic interactions are taken into account. In this case, the individual particles have a uniform micromagnetic structure similar to SD particles although their grain size is above the SD/PSD threshold, but together they form larger vortices with the vortex core outside the individual particles. *Evans et al.* [2006] showed that such a configuration will give rise to FORC distributions with an isolated SD peak. They also documented a higher B_{int} value of 30 mT, but the average width of the paramagnetic ulvöspinel matrix between magnetite particles is only 30 nm, i.e., about half of the particle separation for sample DK0024-2. If this supervortex hypothesis is a valid explanation for the hysteresis behavior of sample DK0023, then

one would expect a much lower B_{int} for the less densely spaced particles. However, because the particles in this sample have a slightly smaller mean diameter of 100 nm but a much larger spacing, they are likely to straddle the threshold between a uniform SD and a vortex micromagnetic state. The presence of both SD as well as PSD magnetizations will give rise to a wide range of coercivities as observed in Figure 11. It is likely that the large spread in the vertical axis, giving rise to the high B_{int} value, is a product of SD and vortex structures being constantly nucleated and denucleated throughout the FORC measurement procedure, and of internal grain interactions in vortex states. For larger grains in PSD or MD states, the spread in the vertical direction is not necessarily representative of intergrain interaction but is instead due to interactions among domains inside a grain [*Pike et al.*, 2001].

[28] Sample DK0011 has the largest B_{int} of the three samples, suggesting a supervortex state. However, because the particle size of this sample (265 nm) is larger than that of the natural sample of *Evans et al.* [2006] (~200 nm) and much larger than sample DK0024-2, the coercivity peak is located further toward the origin of the FORC diagram and the peak does not have isolated concentric SD contours. It is likely that, in this sample, the vertical spread of the FORC distribution is due to a combination of supervortex state formation and internal interdomain interactions.

[29] The sharp T_V at temperatures close to the expected value for all samples indicates that the magnetite is close to stoichiometric. This is corroborated by M_S values of between 91 and 96 A m^2 kg^{-1} that are also close to expected literature values. M_S data were determined on the basis of the total mass of magnetite in each sample as determined from SEM observations. The M_S data therefore provide confirmation that the dry etching process was successful in transferring the desired pattern into the Fe thin film.

[30] The low-temperature remanent magnetization gradually decreases upon warming between 10 K and T_V (Figure 8). This is likely due to a thermal relaxation process. There are several possible mechanisms for this process, for example, thermal relaxation of superparamagnetic (SP) particles, "regular" unpinning and domain reordering associated with heating, i.e., thermal demagnetization, and relaxation of domain walls due to disaccommodation and dislocation creep [*Walz*, 2002; *Muxworthy and Williams*, 2006b]. Interpretation is further complicated in that samples DK0023 and DK0024-2 are above the theoretical SD grain size threshold limit (~70 nm) for stress-free cubic grains above T_V but are below the SD threshold limit for the monoclinic phase (~140 nm) [*Muxworthy and Williams*, 1999]. This suggests that vortex nucleation would be expected at or near T_V in these two samples, which could also contribute to the decrease in remanence below T_V. We exclude thermal relaxation of SP particles as the cause of the remanence decrease for the following reasons. The nominal particle sizes in our samples are significantly above the SP grain size range, so that only contamination by nanoparticulate debris produced by the fabrication process could result in SP behavior. Contamination by SP particles would affect magnetic hysteresis in two ways: the M_S value would increase above the expected literature value and wasp-waisted hysteresis loops would be expected if significant SP behavior is present [*Roberts et al.*, 1995]. M_S is close to the expected value, while we can exclude wasp-waisted hysteresis loops on the basis of the shape parameter σ_{hys} [*Fabian*, 2003], which ranges between −0.21 and −0.37 for our samples (σ_{hys} will have positive values for wasp-waisted hysteresis loops).

6. Conclusions

[31] We have produced a set of nanofabricated two-dimensional magnetite particle arrays with precisely controlled particle sizes between 100 and 265 nm and well-defined interparticle spacings. We have shown how the size and spacing of these particles influence hysteresis parameters and the strength of magnetostatic interactions in relation to magnetic parameters for previously published data from natural and synthetic magnetites. Overall, the stoichiometry of our samples and the ability to precisely control grain size and grain separation make these magnetite particle arrays an ideal material for studying the effects of intergrain magnetostatic interactions in geological materials. Future systematic studies of such nanofabricated samples should enable decoupling of the effects of variations of the key parameters (particle size, particle shape and interparticle spacing) on the recording fidelity of magnetite, and other key rock magnetic minerals.

[32] **Acknowledgments.** The magnetic measurements were performed at the Institute for Rock Magnetism (IRM), Minneapolis. The IRM is funded by the Instrumentation and Facilities Program of the U.S. National Science Foundation, Earth Science Division and by the University of Minnesota. This research was funded by the Natural Environment Research Council (NERC grant NE/C510159/1 to W.W., C.D.W.W., A.P.R., and A.R.M.) and by a Royal Society of Edinburgh/BP Trust Research Fellowship (to D.K.). We thank the technical staff at the James Watt Nanofabrication Centre for assistance in the laboratory and John Chapman for valuable discussions. We benefited from constructive comments by the Associate Editor Alexei Smirnov and by Karl Fabian and Dave Heslop.

References

Abramoff, M. D., P. J. Magelhaes, and S. J. Ram (2004), Image processing with image J, *Biophotonics Int.*, *11*, 36–42.

Argyle, K. S., and D. J. Dunlop (1990), Low-temperature and high-temperature hysteresis of small multidomain magnetites (215–540 nm), *J. Geophys. Res.*, *95*, 7069–7083, doi:10.1029/JB095iB05p07069.

Carvallo, C., A. P. Roberts, R. Leonhardt, C. Laj, C. Kissel, M. Perrin, and P. Camps (2006), Increasing the efficiency of paleointensity analyses by selection of samples using first-order reversal curve diagrams, *J. Geophys. Res.*, *111*, B12103, doi:10.1029/2005JB004126.

Coe, R. S. (1967), The determination of paleointensities of the Earth's magnetic field with emphasis on mechanisms which could cause non-ideal behavior in Thellier's method, *J. Geomagn. Geoelectr.*, *19*, 157–179.

Curtis, A. S. G., N. Gadegaard, M. J. Dalby, M. O. Riehle, C. D. W. Wilkinson, and G. Aitchison (2004), Cells react to nanoscale order and symmetry in their surroundings, *IEEE Trans. Nanobiosci.*, *3*, 61–65, doi:10.1109/TNB.2004.824276.

Dalby, M. J., N. Gadegaard, R. Tare, A. Andar, M. O. Riehle, P. Herzyk, C. D. W. Wilkinson, and R. O. C. Oreffo (2007), The control of human mesenchymal cell differentiation using nanoscale symmetry and disorder, *Nat. Mater.*, *6*, 997–1003, doi:10.1038/nmat2013.

Day, R., M. Fuller, and V. A. Schmidt (1977), Hysteresis properties of titanomagnetites: Grain-size and compositional dependence, *Phys. Earth Planet. Inter.*, *13*, 260–267, doi:10.1016/0031-9201(77)90108-X.

Dunlop, D. J. (1986), Hysteresis properties of magnetite and their dependence on particle size: A test of pseudo-single-domain remanence models, *J. Geophys. Res.*, *91*, 9569–9584, doi:10.1029/JB091iB09p09569.

Dunlop, D. J. (2002), Theory and application of the Day plot (M_{rs}/M_s versus H_{cr}/H_c): 1. Theoretical curves and tests using titanomagnetite data, *J. Geophys. Res.*, *107*(B3), 2056, doi:10.1029/2001JB000486.

Dunlop, D. J., and Ö. Özdemir (1997), *Rock Magnetism: Fundamentals and Frontiers*, 573 pp., Cambridge Univ. Press, Cambridge, U.K.

Evans, M. E., D. Krása, W. Williams, and M. Winklhofer (2006), Magnetostatic interactions in a natural magnetite/ulvöspinel system, *J. Geophys. Res.*, *111*, B12S16, doi:10.1029/2006JB004454.

Fabian, K. (2003), Some additional parameters to estimate domain state from isothermal magnetization measurements, *Earth Planet. Sci. Lett.*, *213*, 337–345, doi:10.1016/S0012-821X(03)00329-7.

Feinberg, J. M., G. R. Scott, P. R. Renne, and H. R. Wenk (2005), Exsolved magnetite inclusions in silicates: Features determining their remanence behavior, *Geology*, *33*, 513–516, doi:10.1130/G21290.1.

Gadegaard, N., S. Thoms, D. S. Macintyre, K. McGhee, J. Gallagher, B. Casey, and C. D. W. Wilkinson (2003), Arrays of nano-dots for cellular engineering, *Microelectron. Eng.*, *67–68*, 162–168, doi:10.1016/S0167-9317(03)00067-4.

Gadegaard, N., M. J. Dalby, M. O. Riehle, and C. D. W. Wilkinson (2008), Optimizing substrate disorder for bone tissue engineering of mesenchymal stem cells, *J. Vac. Sci. Technol. B*, *26*(6), 2554–2557, doi:10.1116/1.2978407.

Harrison, R. J., R. E. Dunin-Borkowski, and A. Putnis (2002), Direct imaging of nanoscale magnetic interactions in minerals, *Proc. Natl. Acad. Sci. U. S. A.*, *99*, 16,556–16,561, doi:10.1073/pnas.262514499.

Hicks, S. E., W. Parkes, J. A. H. Wilkinson, and C. D. W. Wilkinson (1994), Reflectance modeling for in-situ dry etch monitoring of bulk SiO_2 and III–V multilayer structures, *J. Vac. Sci. Technol. B*, *12*, 3306–3310, doi:10.1116/1.587617.

Khamsehpour, B., C. D. W. Wilkinson, and J. N. Chapman (1997), Use of laser reflectometry for end-point detection during the etching of magnetic thin films, *J. Vac. Sci. Technol. A*, *15*, 2069–2073, doi:10.1116/1.580610.

King, J. G. (1996), Magnetic properties of arrays of magnetite particles produced by the method of electron beam lithography (EBL), Ph.D. thesis, 155 pp., Univ. of Edinburgh, Edinburgh, U.K.

King, J. G., W. Williams, C. D. W. Wilkinson, S. McVitie, and J. N. Chapman (1996), Magnetic properties of magnetite arrays produced by the method of electron beam lithography, *Geophys. Res. Lett.*, *23*, 2847–2850, doi:10.1029/96GL01371.

Kong, X., D. Krása, H. P. Zhou, W. Williams, S. McVitie, J. M. R. Weaver, and C. D. W. Wilkinson (2008), Very high resolution etching of magnetic nanostructures in organic gases, *Microelectron. Eng.*, *85*, 988–991, doi:10.1016/j.mee.2007.12.006.

Krása, D., C. Heunemann, R. Leonhardt, and N. Petersen (2003), Experimental procedure to detect multidomain remanence during Thellier-Thellier experiments, *Phys. Chem. Earth*, *28*, 681–687.

Leonhardt, R., D. Krása, and R. S. Coe (2004), Multidomain behavior during Thellier paleointensity experiments: A phenomenological model, *Phys. Earth Planet. Inter.*, *147*, 127–140, doi:10.1016/j.pepi.2004.01.009.

Matsui, N., K. Mashimo, A. Egami, A. Konishi, O. Okada, and T. Tsukada (2002), Etching characteristics of magnetic materials (Co, Fe, Ni) using CO/NH3 gas plasma for hardening mask etching, *Vacuum*, *66*, 479–485, doi:10.1016/S0042-207X(02)00119-7.

Muxworthy, A. R., and A. P. Roberts (2007), First-order reversal curve (FORC) diagrams, in *Encylopedia of Geomagnetism and Paleomagnetism*, edited by D. Gubbins and E. Herrero-Bervera, pp. 266–272, Springer, Dordrecht, Netherlands.

Muxworthy, A. R., and W. Williams (1999), Micromagnetic models of pseudo-single domain grains of magnetite near the Verwey transition, *J. Geophys. Res.*, *104*, 29,203–29,217, doi:10.1029/1999JB900294.

Muxworthy, A. R., and W. Williams (2006a), Critical single-domain/multidomain grain sizes in noninteracting and interacting elongated magnetite particles: Implications for magnetosomes, *J. Geophys. Res.*, *111*, B12S12, doi:10.1029/2006JB004588.

Muxworthy, A. R., and W. Williams (2006b), Low-temperature viscous magnetization of multidomain magnetite: Evidence for disaccommodation contribution, *J. Magn. Magn. Mater.*, *307*, 113–119, doi:10.1016/j.jmmm.2006.03.052.

Muxworthy, A., W. Williams, and D. Virdee (2003), Effect of magnetostatic interactions on the hysteresis parameters of single-domain and pseudo-single-domain grains, *J. Geophys. Res.*, *108*(B11), 2517, doi:10.1029/2003JB002588.

Muxworthy, A., D. Heslop, and W. Williams (2004), Influence of magnetostatic interactions on first-order-reversal-curve (FORC) diagrams: A micromagnetic approach, *Geophys. J. Int.*, *158*, 888–897, doi:10.1111/j.1365-246X.2004.02358.x.

Muxworthy, A. R., J. G. King, and N. Odling (2006), Magnetic hysteresis properties of interacting and noninteracting micron-sized magnetite produced by electron beam lithography, *Geochem. Geophys. Geosyst.*, *7*, Q07009, doi:10.1029/2006GC001309.

Nakatani, I. (1996), Ultramicro fabrications on Fe-Ni alloys using electron-beam writing and reactive-ion etching, *IEEE Trans. Magn.*, *32*, 4448–4451, doi:10.1109/20.538896.

Namatsu, H., Y. Takahashi, K. Yamazaki, T. Yamaguchi, M. Nagase, and K. Kurihara (1998), Three-dimensional siloxane resist for the formation of nanopatterns with minimum linewidth fluctuations, *J. Vac. Sci. Technol. B*, *16*, 69–76, doi:10.1116/1.589837.

Néel, L. (1949), Théorie du traînage magnétique des ferromagnétiques en grains fins avec applications aux terres cuites, *Ann. Geophys.*, *5*, 99–136.

Newell, A. J. (2005), A high-precision model of first-order reversal curve (FORC) functions for single-domain ferromagnets with uniaxial anisotropy, *Geochem. Geophys. Geosyst.*, *6*, Q05010, doi:10.1029/2004GC000877.

Özdemir, Ö., D. J. Dunlop, and B. M. Moskowitz (1993), The effect of oxidation on the Verwey transition in magnetite, *Geophys. Res. Lett.*, *20*, 1671–1674, doi:10.1029/93GL01483.

Pike, C. R., A. P. Roberts, and K. L. Verosub (1999), Characterizing interactions in fine magnetic particle systems using first order reversal curves, *J. Appl. Phys.*, *85*, 6660–6667, doi:10.1063/1.370176.

Pike, C. R., A. P. Roberts, M. J. Dekkers, and K. L. Verosub (2001), An investigation of multi-domain hysteresis mechanisms using FORC diagrams, *Phys. Earth Planet. Inter.*, *126*, 11–25, doi:10.1016/S0031-9201(01)00241-2.

Roberts, A. P., Y. L. Cui, and K. L. Verosub (1995), Wasp-waisted hysteresis loops: Mineral magnetic characteristics and discrimination of components in mixed magnetic systems, *J. Geophys. Res.*, *100*, 17,909–17,924, doi:10.1029/95JB00672.

Roberts, A. P., C. R. Pike, and K. L. Verosub (2000), First-order reversal curve diagrams: A new tool for characterizing the magnetic properties of natural samples, *J. Geophys. Res.*, *105*, 28,461–28,475, doi:10.1029/2000JB900326.

Schmidbauer, E., and R. Keller (1996), Magnetic properties and rotational hysteresis of F_e3O_4 and γ-Fe_2O_3 particles $\sim$ 250 nm in diameter, *J. Magn. Magn. Mater.*, *152*, 99–108, doi:10.1016/0304-8853(95)00446-7.

Schmidbauer, E., and N. Schembera (1987), Magnetic hysteresis properties and anhysteretic remanent magnetization of spherical Fe_3O_4 particles in the grain size range 60–160 nm, *Phys. Earth Planet. Inter.*, *46*, 77–83, doi:10.1016/0031-9201(87)90173-7.

Smirnov, A. V. (2006), Memory of the magnetic field applied during cooling in the low-temperature phase of magnetite: Grain size dependence, *J. Geophys. Res.*, *111*, B12S04, doi:10.1029/2006JB004573.

Thellier, E., and O. Thellier (1959), Sur l'intensité du champ magnétique terrestre dans le passé historique et géologique, *Ann. Geophys.*, *15*, 285–376.

Verwey, E. J. (1939), Electronic conduction of magnetite (Fe_3O_4) and its transition point at low temperature, *Nature*, *144*, 327–328, doi:10.1038/144327b0.

Walz, F. (2002), The Verwey transition—A topical review, *J. Phys. Condens. Matter*, *14*, R285–R340, doi:10.1088/0953-8984/14/12/203.

Williams, W., and D. J. Dunlop (1995), Simulation of magnetic hysteresis in pseudo-single-domain grains of magnetite, *J. Geophys. Res.*, *100*, 3859–3871, doi:10.1029/94JB02878.

Winklhofer, M., and G. T. Zimanyi (2006), Extracting the intrinsic switching field distribution in perpendicular media: A comparative analysis, *J. Appl. Phys.*, *99*(8), 08E710, doi:10.1063/1.2176598.

Zhou, H. P., K. Elgaid, C. Wilkinson, and I. Thayne (2006), Low-hydrogen-content silicon nitride deposited at room temperature by inductively coupled plasma deposition, *Jpn. J. Appl. Phys., Part 1*, *45*, 8388–8392, doi:10.1143/JJAP.45.8388.

N. Gadegaard, C. D. W. Wilkinson, and H. Zhou, Department of Electronics and Electrical Engineering, University of Glasgow, Rankine Building, Oakfield Avenue, Glasgow G12 8LT, UK.

X. Kong, Department of Physics and Astronomy, University of Glasgow, Kelvin Building, Glasgow G12 8QQ, UK.

D. Krása and W. Williams, School of GeoSciences, University of Edinburgh, King's Buildings, West Mains Road, Edinburgh EH9 3JW, UK. (david.krasa@ed.ac.uk)

A. R. Muxworthy, Department of Earth Science and Engineering, Imperial College London, South Kensington Campus, London SW7 2AZ, UK.

A. P. Roberts, National Oceanography Centre, University of Southampton, European Way, Southampton SO14 3ZH, UK.